

SOLAR CELLS

Resolving spatial and energetic distributions of trap states in metal halide perovskite solar cells

Zhenyi Ni^{1*}, Chunxiong Bao^{2*}, Ye Liu^{1,2}, Qi Jiang¹, Wu-Qiang Wu¹, Shangshang Chen¹, Xuezheng Dai¹, Bo Chen¹, Barry Hartweg³, Zhengshan Yu³, Zachary Holman³, Jinsong Huang^{1,2†}

We report the profiling of spatial and energetic distributions of trap states in metal halide perovskite single-crystalline and polycrystalline solar cells. The trap densities in single crystals varied by five orders of magnitude, with a lowest value of 2×10^{11} per cubic centimeter and most of the deep traps located at crystal surfaces. The charge trap densities of all depths of the interfaces of the polycrystalline films were one to two orders of magnitude greater than that of the film interior, and the trap density at the film interior was still two to three orders of magnitude greater than that in high-quality single crystals. Surprisingly, after surface passivation, most deep traps were detected near the interface of perovskites and hole transport layers, where a large density of nanocrystals were embedded, limiting the efficiency of solar cells.

The photovoltaic performance of metal halide perovskites (MHPs) is mainly attributed to their high optical absorption coefficient (1), high carrier mobility (2), long charge-diffusion length (3), and small Urbach energy (4). Defect tolerance in MHPs was initially proposed as one origin for their excellent carrier transport and particular recombination properties, in that most point defects have low formation energy in the bulk of perovskites and do not form deep charge traps (5, 6). Later theoretical studies showed that the structural defects at the material surface and grain boundaries of perovskites can induce deep charge traps, which has guided the development of passivation techniques in perovskite solar cells (7–9), but this was only inferred indirectly. The nonradiative recombination process also leads to the energy loss of the perovskite solar cells, which is closely related to the defect-induced trap states in the perovskites (10, 11). Charge trap states play an important role in the degradation of perovskite solar cells and other devices (12, 13). Knowledge of the distributions of trap states in space and energy is one of the most fundamental ingredients for understanding the impact of the charge traps on charge transport and recombination in perovskite materials and devices.

Thermal admittance spectroscopy (TAS) and thermally stimulated current methods have been broadly applied to measure the energy-dependent trap density of states (tDOS) in perovskite solar cells (14–16). These methods can generally reach a trap depth of ~ 0.55 eV from the conduction or valence band edge,

which is normally deep enough for most low-band gap perovskites that make efficient solar cells. Techniques like surface photovoltage spectroscopy and sub-band gap photocurrent are capable of detecting deeper trap states that exist in wide-band gap perovskites (17–19). Sub-band gap photoluminescence, which was adopted to investigate the properties of luminescent trap states in perovskite (20), and cathodoluminescence were shown to image the nanoscale stoichiometric variations that are related to the traps at the film surface (21). However, these techniques are not readily applied to completed solar cell devices to measure the spatial distribution of trap states. Deep-level defect characterization methods such as deep-level transient spectroscopy are not readily applicable to perovskite devices, because the long biasing times are affected by ion migration in MHPs. Here, we demonstrate that the drive-level capacitance profiling (DLCP) method, an alternate capacitance-based technique, can provide well-characterized spatial distributions of carrier and trap densities in perovskites. We mapped the spatial and energetic distributions of trap states in perovskite single crystals and polycrystalline thin films. A straightforward comparison of the trap densities and distributions in perovskite single crystals and thin films in typical planar-structured solar cells was then conducted.

Drive-level capacitance profiling of perovskites

The DLCP method was developed to study the spatial distribution of defects in the band gap of amorphous and polycrystalline semiconductors, including amorphous silicon (Si) (22), $\text{CuIn}_{1-x}\text{Ga}_x\text{Se}_2$ (23), and $\text{Cu}_2\text{ZnSnSe}_4$ (24). With the junction capacitance measurements, DLCP can directly determine the carrier density that includes both free carrier density and trap density within the band gap of the semiconductors and their distributions in space and energy (Fig. 1A and supplementary materials). The trap density was estimated by subtracting the

estimated free carrier density, which was measured at high alternating current (ac) frequencies when the measured carrier densities saturate with the further increase of the ac frequency, from the total carrier density measured at the low ac frequency. This technique allowed us to derive the energetic distribution (E_ω) of trap states by tuning the frequency of the ac bias (δV) or temperature (T) and the position of trap states in real space by changing the direct current (dc) bias that was applied to the depletion region of the junction. As long as the spatial property of the semiconductor did not change dramatically, the differences in the profiling distance closely approximated the actual changes in the position where trap states responded to the capacitance, thus reflecting the change of the trap density in real space. In principle, DLCP can have a high resolution because the depletion edge can be continuously tuned by the applied dc bias. However, the profiling distance within the real devices was affected by the nonflat depletion interfaces caused by either the roughness or the heterogeneity of the materials, which could compromise the resolution of the profiling distance.

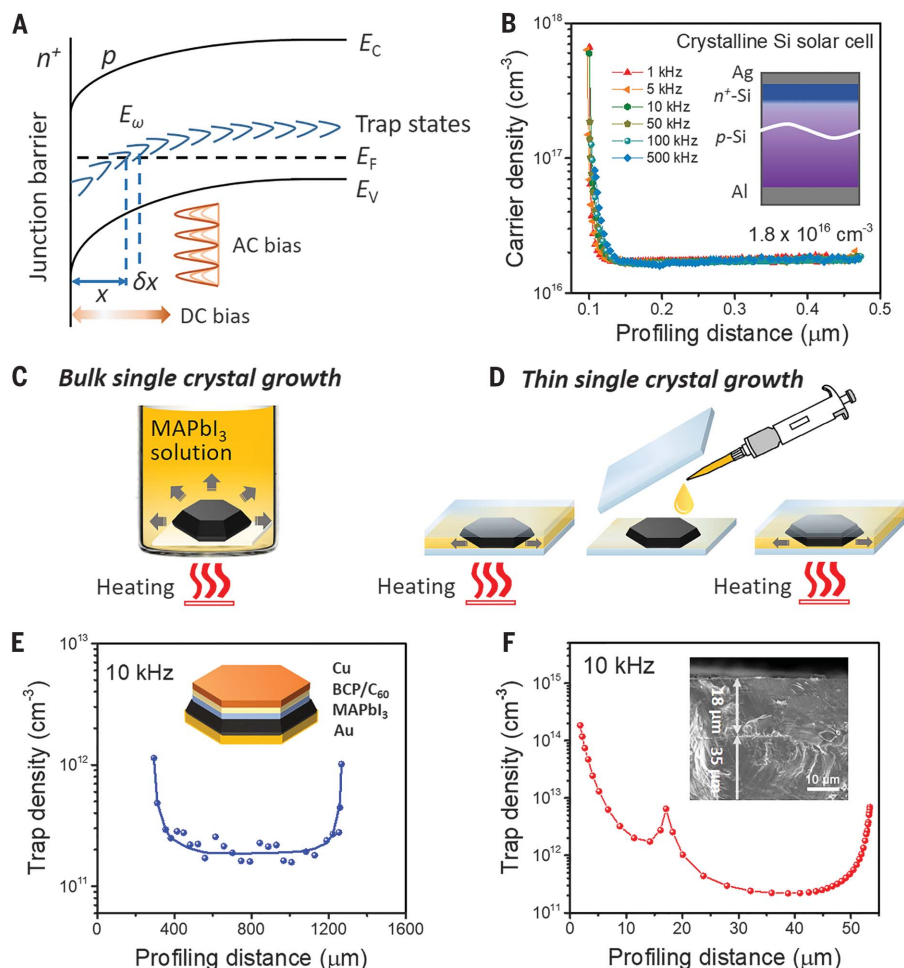
To validate the accuracy of the carrier density measured by DLCP, we first performed DLCP measurements on a Si solar cell, which was fabricated based on a p-type (~ 0.94 ohm-cm with the dopant concentration of $\sim 1.6 \times 10^{16} \text{ cm}^{-3}$) crystalline Si (p-Si) wafer with a heavily n-type diffusion layer Si (n^+) on top (details in the materials and methods section of the supplementary materials). The carrier density was calculated from the derived linear and nonlinear capacitive coefficients C_0 and C_1 , respectively, by fitting the C - δV plots at different dc biases and ac frequencies (fig. S1). When the profiling distance is $>0.15 \mu\text{m}$, which should reach the interior of the p-Si, the carrier densities measured at different ac frequencies (1 to 500 kHz) were basically the same (Fig. 1B), indicating negligible contributions of the trap states to the junction capacitance. In this case, the measured carrier density should be the free carrier concentration of the p-Si wafer, which was read to be $\sim 1.8 \times 10^{16} \text{ cm}^{-3}$ from the DLCP measurement. This value was consistent with the dopant concentration of the p-Si wafer derived from the conductivity measurement, validating the accuracy of the carrier density measured by DLCP.

Because the profiling of carrier and trap densities by DLCP relied on the sweeping of a depletion region edge across a device from one electrode to the counter electrode, it was critical to understand the location of the junction(s) in typical planar-structured perovskite solar cells with the device structure of indium tin oxide (ITO)/poly[bis(4-phenyl)(2,4,6-trimethylphenyl)amine] (PTAA) (15 nm)/perovskite/fullerene (C_{60}) (25 nm)/bathocuproine (BCP)/copper (Cu). It was found that

¹Department of Applied Physical Sciences, University of North Carolina, Chapel Hill, NC 27599, USA. ²Department of Mechanical and Materials Engineering and Nebraska Center for Materials and Nanoscience, University of Nebraska–Lincoln, Lincoln, NE 68588, USA. ³School of Electrical, Computer, and Energy Engineering, Arizona State University, Tempe, AZ 85287, USA.

*These authors contributed equally to this work.

†Corresponding author. Email: jhuang@unc.edu



these perovskite solar cells essentially had a n^+ -p junction formed between the C_{60} and the perovskites (figs. S2 and S3). Another concern with DLCP measurements of MHPs is the role of ion migration. During the DLCP measurement, a positive dc bias was usually applied onto perovskite devices, which actually partially compensated for the built-in field in the devices. Thus, the field in the device was always less than the built-in field, which should, in principle, minimize ion migration. In addition, each DLCP scan takes only a few minutes, and we confirmed the negligible influence of the ion migration on the DLCP measurement of these hysteresis-free perovskite solar cells by performing consecutive forward and backward scans of the dc biases (fig. S4).

We synthesized bulk $\text{CH}_3\text{NH}_3\text{PbI}_3$ (MAPbI₃) single crystals using the inverse solubility method (Fig. 1C). The DLCP measurements were performed on a MAPbI₃ single-crystal device with a structure of gold (Au)/MAPbI₃/C₆₀/BCP/Cu, where both sides of the crystal were polished to remove the defective surface layers (fig. S5). A symmetric distribution of the trap density was observed (Fig. 1E), in a good agreement with the structural symmetry of

the double-side polished MAPbI₃ single crystal. This result demonstrated the spatial profiling of trap densities in MAPbI₃ single crystals by DLCP. The trap density near the interface region was ~ 10 -fold greater than that inside the MAPbI₃ single crystal. This difference indicated that dangling bonds at the surface of the crystal form charge traps.

To determine whether the profile depth corresponded to the physical material depth, we made a device with double-layer MAPbI₃ thin single crystals so that we knew the location of the charge traps (Fig. 1D). We first synthesized a 35- μm -thick MAPbI₃ thin single crystal on a PTAA/ITO substrate using the space-confined growth method (25) and then interrupted the growth by exposing the top surface of the thin single crystal to air for 1 min before continuing the crystal growth. This step created a distinct boundary between the two layers [cross-sectional scanning electron microscope (SEM) image in the inset of Fig. 1F] that should be rich in charge traps. This defective interface was located 18 μm below the surface of the top subcrystal (inset of Fig. 1F). The profiled trap density of this device (Fig. 1F) showed a peak in the trap density at the profiling distance of 18 μm .

Fig. 1. DLCP technique. (A) Schematic of band bending of a p-type semiconductor with deep trap states in an n^+ -p junction. x denotes the distance from the junction barrier where the traps may be able to dynamically change their charge states with the ac bias δV . δx denotes the differential change of x with respect to δV . E_ω is the demarcation energy determined by $E_\omega = kT \ln(\omega_0/\omega)$ (where k is the Boltzmann's constant). E_C , E_V , and E_F indicate the conduction band edge, valence band edge, and Fermi level, respectively. (B) Dependence of the carrier density on the profiling distance of a Si solar cell at different ac frequencies measured by DLCP. The inset shows the schematic of the device structure. (C) Schematic of the synthesis of a bulk MAPbI₃ single crystal in an open-air solution. (D) Schematic of the synthesis of a double-layer MAPbI₃ thin single crystal using the space-confined growth method. (E) Dependence of the trap density on the profiling distance of a MAPbI₃ single crystal measured by DLCP. The inset shows the device structure. (F) Dependence of the trap density on the profiling distance of a double-layer MAPbI₃ thin single crystal. The inset shows the cross-sectional SEM image of the double-layer MAPbI₃ thin single crystal. The thicknesses of the top and bottom single crystals were 18 and 35 μm , respectively.

Trap distributions in MAPbI₃ thin single crystals

We studied the trap distribution in perovskite single-crystal solar cells. Perovskite solar cells made from a single-crystal perovskite could, in principle, have a power conversion efficiency (PCE) approaching the Shockley-Queisser limit (usually 33.7% for a single junction) because of the extremely low defect density and long carrier diffusion length (3, 26). However, the highest PCE of the first-reported MAPbI₃ single-crystal solar cell was only 17.9% (25). A more recent study reported 21.1% (27), which is still far lower than that of polycrystalline solar cells. Initial studies indicate that thin crystals formed by the space-confined growth method have a smaller carrier diffusion length (10 to 20 μm) than that of thick bulk crystals (175 μm), which do not suffer from the impact of substrates. (25). However, the underlying mechanism limiting carrier diffusion in thin crystals was not clear.

We conducted DLCP measurements to understand the relationship of trap density and distribution with synthetic-crystal methods. Figure 2A shows the spatial distribution of carrier densities throughout a typical MAPbI₃

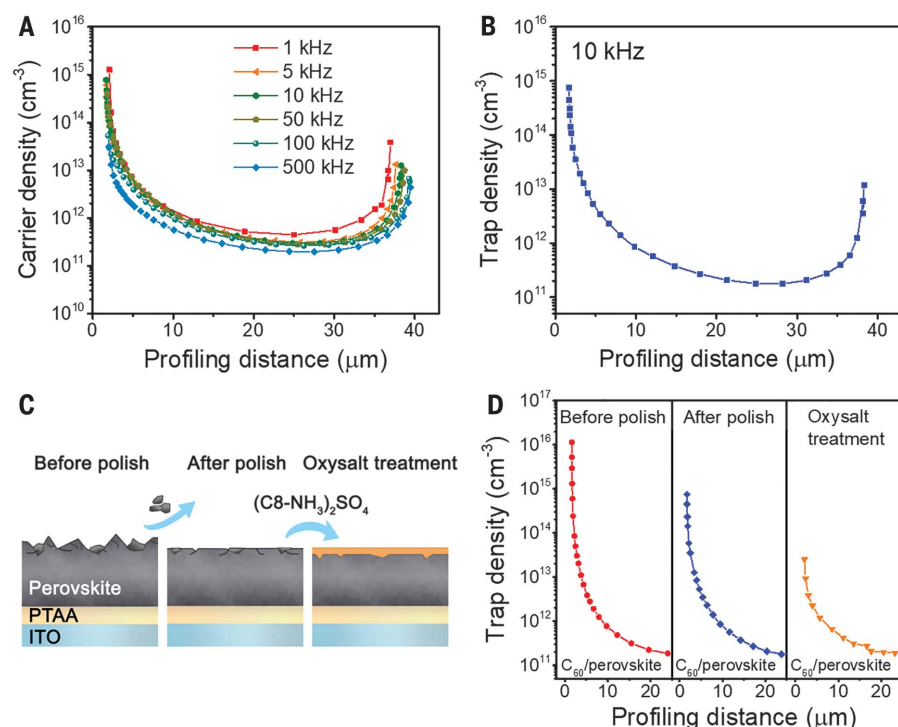


Fig. 2. Spatial distributions of trap states in a MAPbI₃ thin single crystal. (A) Dependence of the carrier density on the profiling distance of a 39-μm-thick MAPbI₃ thin single crystal at different ac frequencies, as measured by DLCP. (B) Dependence of the trap density on the profiling distance of a MAPbI₃ thin single crystal measured at an ac frequency of 10 kHz. The carrier density measured at 500 kHz is regarded as free carriers. (C) Schematics of a MAPbI₃ thin single crystal on a PTAA/ITO substrate before mechanical polish, after mechanical polish, and after oxysalt [(C₈-NH₃)₂SO₄] treatment. (D) Trap density near the junction barrier of a MAPbI₃ thin single crystal before mechanical polish, after mechanical polish, and after oxysalt treatment.

thin single crystal that was synthesized by the space-confined growth method in the device with a structure of ITO/PTAA/MAPbI₃ (39 μm)/C₆₀/BCP/Cu at different ac frequencies. The carrier density increased with the decrease in ac frequency, indicating the existence of charge traps in the MAPbI₃ thin single crystal that contributed to the junction capacitance at low ac frequencies (large E_w). Figure 2B shows a representative spatial distribution of trap densities in the MAPbI₃ thin single crystal at the ac frequency of 10 kHz by subtracting the free carrier density measured at high ac frequencies from the total carrier density measured at the 10-kHz frequency. As the profiling position changed from the interfaces to the interior of the single crystal, the trap density decreased. This result indicated that the majority of the trap states were near the surface of the MAPbI₃ thin single crystal. The free carrier density was also higher near the surface of the MAPbI₃ thin single crystal (Fig. 2A), indicating that both self-doping and trap states are caused by defects, most likely, of different kinds.

To figure out how sensitive DLCP is to the change in the trap density close to the surface

of the MAPbI₃ thin single crystals, we varied the trap density at the top surface (C_{60} side) of the MAPbI₃ thin single crystal by polishing and treating it with (C₈-NH₃)₂SO₄ before performing DLCP measurements (Fig. 2C). Recent work has demonstrated that surface wrapping with oxysalt can effectively passivate the defective surface of perovskites with the wide-band gap oxysalts (28). The trap density was reduced by about one order of magnitude after polishing the top surface of the MAPbI₃ thin single crystal and was further reduced after the surface treatment with (C₈-NH₃)₂SO₄ (Fig. 2D). Because DLCP only measured the carrier density in the junction area, this result also validates the finding that the measured junction is located at the perovskite/ C_{60} interface. Thus, the interface regions of the perovskite/ C_{60} and the perovskite/PTAA were readily distinguished in the spatial distribution profiling of trap states.

The trap density distribution in the MAPbI₃ thin single crystal synthesized by the space-confined method was quite different from that in the bulk crystal. The trap densities varied by up to five orders of magnitude, and the trap density near both surfaces was two to four

orders of magnitude higher than that in the bulk crystals. The trap density decreased gradually toward the center of the crystal, and its distribution along the normal direction was not symmetric, despite both surfaces of the thin single crystal contacting PTAA/ITO during the growth process. To understand these differences, we synthesized MAPbI₃ thin single crystals with different thicknesses (10 to 39 μm) and investigated the variation of the trap density distribution with the change in the crystal thicknesses (Fig. 3A). The minimal bulk trap density ($N_{T \min}$) inside the MAPbI₃ thin single crystal, which occurred near the center of the crystal, decreased from $\sim 3.2 \times 10^{12}$ to 1.9×10^{11} cm⁻³ as the thickness of the thin single crystal increased from 10 to 32 μm and began to saturate with increased crystal thickness (Fig. 3B). The saturated $N_{T \min}$ of 1.8×10^{11} cm⁻³ approached that of the bulk MAPbI₃ single crystal synthesized in open-air solution (Fig. 1E). These results indicate that there is a critical crystal thickness for the MAPbI₃ thin single crystals synthesized by the space-confined method, below which the trap density inside the crystals was substantially higher than that in the bulk crystal. We speculate that the space-confined method may induce defects through the strain imposed by the mismatch of the substrates and the crystals during growth and that the strain inside the crystals may be released with the increase in crystal thickness. Another possible mechanism for defect formation is that the substrates affect the transport of ions for micrometer-scale channels. The microfluid would undergo laminar flow at low flow rates near the substrates (inset of Fig. 3B) (29). For the thinner single crystals, the averaged velocity of the solution flow would be reduced owing to the confinement of the boundary layer by the small space, resulting in not enough ions being delivered to the crystal for growth. Insufficient ion delivery to the crystal surface would create a deficiency for one type of ions, or misfit defects.

Similarly, the trap density near the MAPbI₃/PTAA interface also decreased with the increase in the crystal thickness and was essentially constant with further increases in crystal thickness (Fig. 3A). However, the imposed strains between the two sides of the single crystal and the substrates were not always identical because of the subtle difference in the roughness of the two PTAA/ITO substrates, which led to the different defect density distributions at the two surfaces of the crystals. The side with a higher defect density may have a weaker contact with the PTAA/ITO substrate, making the PTAA/ITO substrate easier to be peeled off from this side. It is this defective side that C_{60} was deposited on during the device fabrication process that was used. Moreover, the distribution of trap density in MAPbI₃ thin single crystals depended not only on the spacing of the two

substrates but also on the substrate upon which the crystals grew. The latter also affects the strain inside the crystals and the microfluid of the precursor solution, as evidenced by the difference in the trap densities measured in the top and bottom subcrystals of the double-layer sample in Fig. 1F. The top subcrystal had a much higher $N_{T\min}$ than the bottom MAPbI₃ thin single crystal grown directly on a PTAA/ITO substrate (Fig. 3A).

We examined further the tDOS in energy space in the MAPbI₃ thin single crystal with a thickness of 39 μm . To verify the effectiveness of the DLCP in determining the tDOS, we derived the tDOS in the MAPbI₃ thin single crystal by both TAS and DLCP methods, because TAS is a well-established method to determine the tDOS in perovskite devices (15). The temperature-dependent differential capacitance spectra ($-f\text{d}C/\text{d}f$, where f is the frequency of the ac bias) and the Arrhenius plot of the characteristic frequencies with respect to the temperature [$\ln(\omega/T^2)-1/T$] of the device are shown in fig. S6. Figure 3C shows the E_0 -dependent N_T for the MAPbI₃ thin single crystal measured by TAS. For the DLCP measurement, the tDOS could be estimated by the derivative of the carrier density with respect to E_0 , that is, $N_T(E_0) = \text{d}N/\text{d}(E_0)$. As the profiling distance was scanned from one side of the single crystal to the other, the energy distribution and spatial distribution of the trap states in the MAPbI₃ thin single crystal were mapped (Fig. 3D).

The tDOS measured by DLCP exhibited a similar feature to that measured by TAS (fig. S7). Both tDOS spectra showed three trap bands with E_0 values of 0.27 eV (zone I), 0.35 eV (zone II), and greater than 0.40 eV (zone III). Previous studies speculated that the deep trap states were mainly related to the surface defects of the perovskite and that shallower trap states were more likely from inside the perovskite (15). The spatial and energy distributions of the tDOS in perovskites (Fig. 3D) indicated that the deep trap density at the MAPbI₃/PTAA interface was >100-fold higher than inside the MAPbI₃ thin single crystal, whereas the shallow trap density at the MAPbI₃/PTAA interface was barely higher than those inside the single crystal. Deep traps were mainly located at the surface region of the MAPbI₃ thin single crystals, whereas the shallower traps were prevalent throughout the entire single crystals. This difference indicated their different origins, that is, shallow trap bands I and II may form from point defects in the bulk and deep trap band III originated from the dangling bonds at the material surface. The measured carrier densities near the MAPbI₃/C₆₀ interface at the ac frequencies from 1 to 50 kHz were quite near each other (Fig. 2A), indicating a low deep trap density of states near the MAPbI₃/C₆₀ interface caused by the passivation effect of C₆₀.

Trap distributions in polycrystalline perovskite films

The spatial and energetic distributions of trap states in polycrystalline perovskite thin films are crucial to understanding the performance of those solar cells. We first performed DLCP measurement on a typical planar-structured perovskite thin-film solar cell with the device structure of ITO/PTAA/MAPbI₃/C₆₀/BCP/Cu, which has a typical PCE of 17.8% (table S1). The measured trap density distribution and tDOS mapping in the MAPbI₃ thin film are shown in fig. S8. The MAPbI₃ polycrystalline thin film shows a similar feature of trap distribution with the thin single crystals in which most of the deep trap states (trap band III) are located close to the MAPbI₃/PTAA interface. Then, we carried out DLCP measurement on a high-performance solar cell with the device structure of ITO/PTAA/Cs_{0.05}[HC(NH₂)₂]_{10.70}(CH₃NH₃)_{0.25}PbI₃(Cs_{0.05}FA_{0.70}MA_{0.25}PbI₃)/C₆₀/BCP/Cu, in which the perovskite thin films were modified with the additive of 1,3-diaminopropane (30). The open circuit voltage

(V_{OC}), short-circuit current density (J_{SC}), fill factors (FF), and PCE of the solar cell were 1.15 V, 23.4 mA cm⁻², 77.3%, and 20.8%, respectively (Fig. 4A). The spatial distribution of the carrier densities in the Cs_{0.05}FA_{0.70}MA_{0.25}PbI₃ solar cell is shown in fig. S9. The differences in the carrier densities measured at different ac frequencies revealed the presence of trap states in these perovskite thin films. The trap density at the perovskite/C₆₀ interface was about 10-fold lower than that at the perovskite/PTAA interface (fig. 4B), which might be caused by the passivation of C₆₀ on the surface defects of the perovskite thin film (15, 31). Both interfaces had a higher defect density compared with the interior of the perovskite films.

In the tDOS spectrum of the Cs_{0.05}FA_{0.70}MA_{0.25}PbI₃ solar cell measured by TAS (Fig. 4C), the attempt-to-escape angular frequency ω_0 was derived from the temperature-dependent C - f measurements, as detailed in the materials and methods. The tDOS spectrum contained three different trap centers, dividing the spectrum into three energy bands (marked as I, II, and

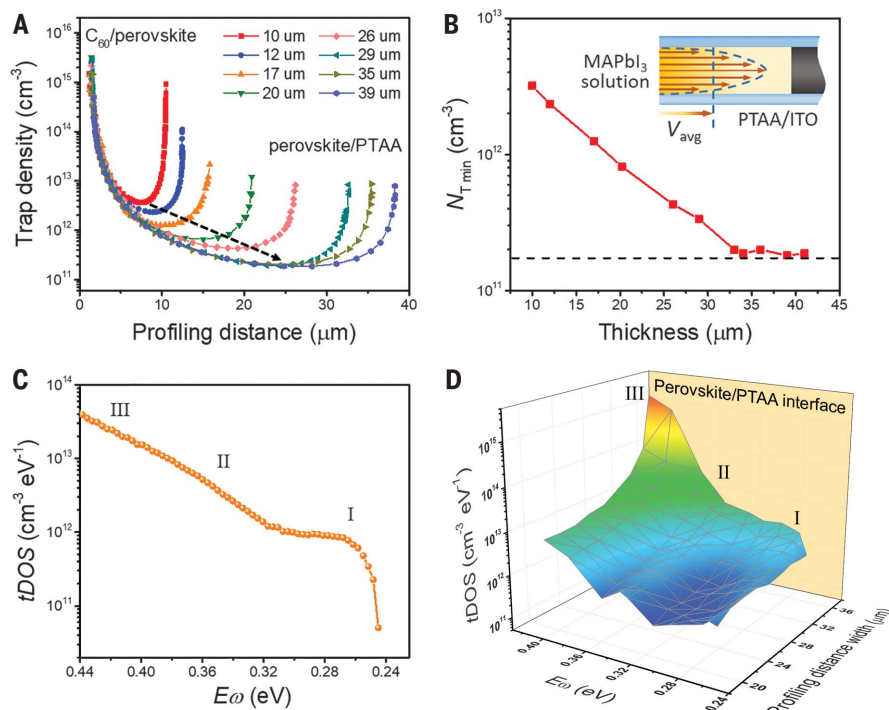


Fig. 3. Thickness-dependent trap density distributions in MAPbI₃ thin single crystals. (A) Dependence of the trap densities on the profiling distances of MAPbI₃ thin single crystals with different crystal thicknesses measured at an ac frequency of 10 kHz. The location of the MAPbI₃/C₆₀ interface for each crystal is aligned for comparison. The black dashed arrow indicates the trend of the change of minimal trap density $N_{T\min}$ in MAPbI₃ single crystals with different thicknesses. (B) Dependence of the $N_{T\min}$ in the MAPbI₃ thin single crystal on the crystal thickness. The horizontal dashed line indicates the $N_{T\min}$ value in a bulk MAPbI₃ single crystal. The inset shows a schematic of the laminar flow of the precursor solution between two PTAA/ITO glasses during the growth of the crystal. The arrows denote the direction of the laminar flow of the precursor solution, and the length of the arrow denotes the laminar flow velocity. (C) tDOS of a MAPbI₃ thin single crystal, as measured by the TAS method. The thickness of the MAPbI₃ thin single crystal was 39 μm . (D) Spatial and energy mapping of the densities of trap states in the MAPbI₃ thin single crystal, as measured by DLCP.

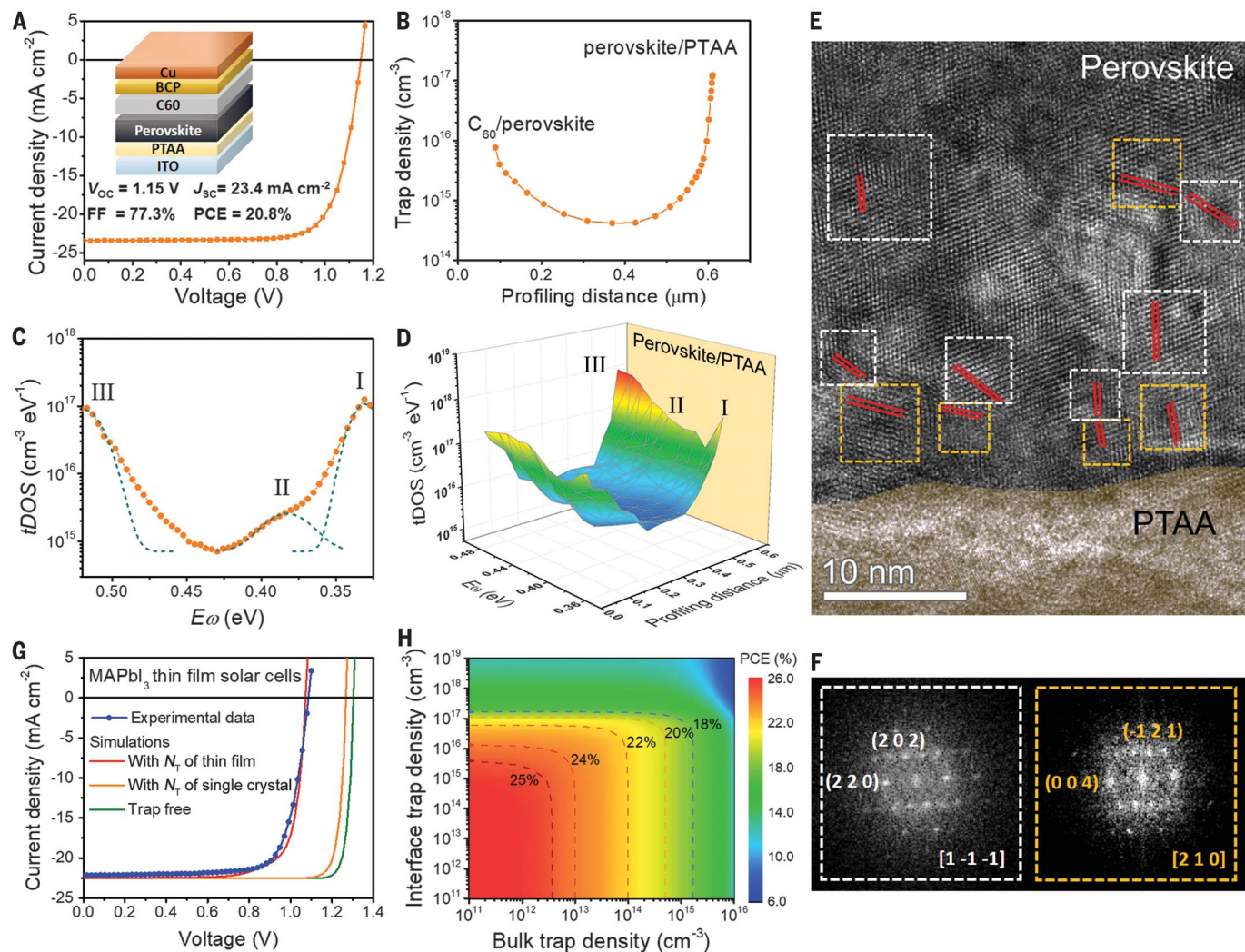


Fig. 4. Spatial and energetic distributions of trap states in perovskite thin films. (A) J-V curve of the $\text{Cs}_{0.05}\text{FA}_{0.70}\text{MA}_{0.25}\text{PbI}_3$ thin-film solar cells. The inset shows the device structure. (B) Dependence of the trap density on the profiling distance for the perovskite thin film in the solar cell measured at an ac frequency of 10 kHz. (C) tDOS of the perovskite thin-film solar cell, as measured by the TAS method. (D) Spatial and energy mapping of the densities of trap states of the perovskite thin film in the solar cell, as measured by DLCP. (E) Cross-sectional HR-TEM image of the stack of perovskite and PTAA. The dashed squares mark the

areas where the fast Fourier transforms of the lattices were performed, with white and yellow indicating zone axes of $[1\ -1\ -1]$ and $[2\ 1\ 0]$, respectively. The red lines denote the orientation of the facets. (F) Fast Fourier transforms of the areas indicated in (E). (G) Measured and simulated J-V curves of planar-structured solar cells based on MAPbI_3 polycrystalline thin films. The thin-film (single crystal) bulk and interface trap densities were adopted for the simulations. (H) Dependence of the PCE of the MAPbI_3 thin-film solar cell on the bulk and interface trap densities. The dashed lines denote the contour lines of certain PCE values, which are noted.

Table 1. Comparison of the minimal bulk trap densities and the interface trap densities between perovskite single crystals and thin films. The interconnected layers are listed in parentheses. The trap densities are calculated at an ac frequency of 10 kHz. The interface trap density values vary depending on different surface and interface conditions.			
Perovskite material	Minimal bulk trap density ($N_{T\ min}$) (cm^{-3})	Interface trap density (cm^{-3})	
MAPbBr_3 single crystal (bulk)	6.5×10^{10}	1.8×10^{12} (C_{60})	1.8×10^{12} (Au)
MAPbI_3 single crystal (bulk)	1.8×10^{11}	1.2×10^{12} (C_{60})	1.2×10^{12} (Au)
MAPbI_3 single crystal (thin)	1.9×10^{11} to 3.2×10^{12}	2.0×10^{13} to 1.1×10^{16} (C_{60})	1.5×10^{13} to 1.0×10^{15} (PTAA)
$\text{Cs}_{0.05}\text{FA}_{0.70}\text{MA}_{0.25}\text{PbI}_3$ film	4.3×10^{14}	8.6×10^{15} (C_{60})	1.2×10^{17} (PTAA)
$\text{Rb}_{0.05}\text{Cs}_{0.05}\text{FA}_{0.75}\text{MA}_{0.15}\text{Pb}(\text{I}_{0.95}\text{Br}_{0.05})_3$ film	5.7×10^{14}	2.0×10^{16} (C_{60})	1.1×10^{17} (PTAA)
$\text{FA}_{0.92}\text{MA}_{0.08}\text{PbI}_3$ film	7.9×10^{14}	1.9×10^{16} (C_{60})	9.0×10^{16} (PTAA)
MAPbI_3 film	9.2×10^{14}	2.2×10^{16} (C_{60})	1.2×10^{17} (PTAA)
$\text{Cs}_{0.05}\text{FA}_{0.8}\text{MA}_{0.15}\text{Pb}_{0.5}\text{Sn}_{0.5}(\text{I}_{0.85}\text{Br}_{0.15})_3$ film	1.2×10^{15}	1.5×10^{16} (C_{60})	1.1×10^{17} (PTAA)

III). The trap distributions in bands I, II, and III of the perovskite thin film are centered at ~0.33, 0.38, and 0.52 eV, respectively. The spatial mapping of the tDOS in the perovskite thin film (Fig. 4D) revealed that the tDOSs at both interface regions were >100-fold higher than that in the film. In addition, deep traps in band III were more localized at the perovskite/PTAA interface, whereas shallower traps in bands I and II were enriched at both interfaces. This result showed that the perovskite surfaces of polycrystalline films were rather defective (31).

To understand the origin of the high deep trap density at the perovskite/TPAA interface, we examined this region by high-resolution transmission electron microscopy (HR-TEM). As shown in Fig. 4, E and F, the lattice had basically the same orientation with the zone axis of [1 -1 -1] in the grain interior, whereas there were a large number of small crystals with sizes of a few nanometers and different orientations (zone axis of [2 1 0]) with respect to the grain interior at the region near the PTAA/perovskite interface. At least 10 samples were examined with different perovskite compositions. All of them had very similar morphology, confirming the heterogeneity of the perovskite films in the vertical direction (32), which we believe was caused by the deposition method-related grain-growth behavior that made the interface between the perovskite and the PTAA rather defective and rich in charge trap centers. Given the excellent passivation effect of C_{60} on the deep trap states at the perovskite surface (33), the remaining deep trap states were mainly located near the perovskite/PTAA interface, which might limit the efficiency of the perovskite thin-film solar cells.

Perovskite single crystals versus polycrystalline films

To find out the differences between the trap density distributions in perovskite single crystals and polycrystalline thin films and in those with different compositions, we measured the $N_{T\min}$ and the interface trap densities in several perovskite single crystals and polycrystalline thin films with different compositions (Table 1). The bulk MAPbI₃ or MAPbBr₃ single crystal showed a quite low $N_{T\min}$ ($<2.0 \times 10^{11} \text{ cm}^{-3}$) which increased to $3.0 \times 10^{12} \text{ cm}^{-3}$ in MAPbI₃ thin single crystals, depending on their growth conditions. However, these values are still two to three orders of magnitude lower than that in MAPbI₃ polycrystalline thin films, which are generally formed by a very quick thin-film coating process. In addition, our current results signify the importance of proper surface-modification processes (mechanical polishing and oxysalt treatment) to reduce trap densities in perovskite single crystals. Similar scenarios could be applied to polycrystalline thin films to reduce the interface trap densities.

Table 1 also lists the $N_{T\min}$ and the interface trap densities of several typical polycrystalline perovskite thin films used in planar-structured solar cells, including Cs_{0.05}FA_{0.70}MA_{0.25}PbI₃, Rb_{0.05}Cs_{0.05}FA_{0.75}MA_{0.15}Pb(I_{0.95}Br_{0.05})₃, FA_{0.92}MA_{0.08}PbI₃, MAPbI₃, and Cs_{0.05}FA_{0.8}MA_{0.15}Pb_{0.5}Sn_{0.5}(I_{0.85}Br_{0.15})₃. The current density-voltage (J - V) curves and trap density distributions of the solar cells fabricated based on these films are shown in fig. S10. The corresponding parameters of device performance are listed in table S1. Among these configurations, the Cs_{0.05}FA_{0.70}MA_{0.25}PbI₃-based solar cell exhibited the highest PCE of 20.8% after optimizing the fabrication processes (30) and had the lowest $N_{T\min}$ of $\sim 4.0 \times 10^{14} \text{ cm}^{-3}$, which was still more than two orders of magnitude greater than that in high-quality single crystals. For the perovskite solar cells fabricated based on the other compositions without comprehensive optimizations, the Rb_{0.05}Cs_{0.05}FA_{0.75}MA_{0.15}Pb(I_{0.95}Br_{0.05})₃-based solar cell showed a relatively high PEC of 19.6%, whereas FA_{0.92}MA_{0.08}PbI₃ and MAPbI₃ showed lower PCEs of ~18.0%. Accordingly, the $N_{T\min}$ in Rb_{0.05}Cs_{0.05}FA_{0.75}MA_{0.15}Pb(I_{0.95}Br_{0.05})₃ was moderately lower than that in FA_{0.92}MA_{0.08}PbI₃ and MAPbI₃. The tin-incorporated Cs_{0.05}FA_{0.8}MA_{0.15}Pb_{0.5}Sn_{0.5}(I_{0.85}Br_{0.15})₃ film showed the highest $N_{T\min}$ of $\sim 1.2 \times 10^{15} \text{ cm}^{-3}$ among all the configurations, reflecting the relative defective nature of tin-containing thin films.

The trend of the variation in the PCE of these solar cells was basically in accordance with the change in the $N_{T\min}$ in different perovskite thin films. This finding signifies the importance of reducing the trap densities in the perovskite thin films for enhancing the device performances. Our current results demonstrate that intrinsic trap densities in perovskite polycrystalline thin films were closely related to the film compositions as well as the film fabrication process. For all the perovskite thin-film compositions, the interface trap density was in the range of $\sim 9.0 \times 10^{15}$ to $2.0 \times 10^{17} \text{ cm}^{-3}$, depending on the type of the charge transport layers. Overall, the trap density at the perovskite/PTAA interface was higher than that at the perovskite/ C_{60} interface because of the formation of large amounts of small crystals near the perovskite/PTAA interface. This morphology points out an important direction to explore for further boosting the performance of perovskite solar cells or other electronic devices by reducing the trap density at the perovskite/PTAA interfaces.

Relationship of trap density and solar cell efficiency

We used the solar cell capacitance simulator to simulate both thin-film and single-crystal perovskite solar cells with varied trap densities. We first used the trap density and distribution measured by DLCP and TAS, which is detailed

in fig. S11 and tables S2 and S3, to simulate a MAPbI₃ thin-film solar cell. Here, the capture cross sections of the bulk and interface trap states were determined by a global fitting of the experimental J - V curves (fig. S12). Figure 4G shows the simulated J - V curve of the MAPbI₃ thin-film solar cell with a bulk trap density of $5.0 \times 10^{14} \text{ cm}^{-3}$ and interface trap density of $1.0 \times 10^{17} \text{ cm}^{-3}$ obtained from the polycrystalline thin films, which was near the measured value. We simulated temperature-dependent J - V curves of the MAPbI₃ thin-film solar cell. As shown in fig. S13, the simulated J - V curves agree well with the measured J - V curves at different temperatures, which indicates that the DLCP measurement range of traps is deep enough to predict the behavior of these solar cells. After reducing only the bulk trap density to $1.0 \times 10^{13} \text{ cm}^{-3}$, the value attainable in single-crystalline MAPbI₃, the PCE increased to 20.0% and saturated with any further decrease in the bulk trap density (Fig. 4H and fig. S14). This saturated PCE was mainly limited by the large interface trap density. If the interface trap density was reduced to that in a MAPbI₃ thin single crystal ($2.0 \times 10^{15} \text{ cm}^{-3}$), the PCE could be further enhanced to 25.4%, which is near the PCE of 26.6% for a trap-free MAPbI₃ thin-film solar cell (Fig. 4G). Simulation of single-crystal solar cells also gave data that were a good match to the experimental data (27), which again showed that the PCE of the MAPbI₃ single-crystal solar cell could be further improved to 26.8% once the interface trap densities are reduced to that of the bulk trap density (fig. S15).

Lower-band gap perovskites are being studied to harvest more sunlight, so we simulated perovskite thin-film solar cells with band gaps of 1.50 and 1.47 eV, which correspond to the compositions of FA_{0.92}MA_{0.08}PbI₃ and FAPbI₃ (if it can be stabilized), respectively (34, 35). Assuming that these materials have the same trap densities (a bulk trap density of $5.0 \times 10^{14} \text{ cm}^{-3}$ and interface trap density of $1.0 \times 10^{17} \text{ cm}^{-3}$) and capture cross sections as regular polycrystalline MAPbI₃ thin films, the devices showed PCEs of 22.5 and 22.8%, respectively (fig. S16). The efficiencies could be further increased to 27.7 and 28.4%, respectively, when the trap densities in the thin film are substantially reduced to be the same as those in single crystals.

REFERENCES AND NOTES

1. N.-G. Park, *Mater. Today* **18**, 65–72 (2015).
2. L. M. Herz, *ACS Energy Lett.* **2**, 1539–1548 (2017).
3. Q. Dong et al., *Science* **347**, 967–970 (2015).
4. C. Gehrman, D. A. Egger, *Nat. Commun.* **10**, 3141 (2019).
5. S. B. Zhang, S.-H. Wei, A. Zunger, *Phys. Rev. Lett.* **78**, 4059–4062 (1997).
6. K. X. Steiner et al., *ACS Energy Lett.* **1**, 360–366 (2016).
7. W.-J. Yin, T. Shi, Y. Yan, *Appl. Phys. Lett.* **104**, 063903 (2014).
8. C. Eames et al., *Nat. Commun.* **6**, 7497 (2015).
9. A. Walsh, D. O. Scanlon, S. Chen, X. G. Gong, S. H. Wei, *Angew. Chem. Int. Ed.* **54**, 1791–1794 (2015).

10. G. J. Wetzelaer *et al.*, *Adv. Mater.* **27**, 1837–1841 (2015).
 11. W. Tress *et al.*, *Adv. Energy Mater.* **5**, 1400812 (2015).
 12. J. M. Ball, A. Petrozza, *Nat. Energy* **1**, 16149 (2016).
 13. T. Leijtens *et al.*, *Adv. Energy Mater.* **5**, 1500962 (2015).
 14. C. Ran, J. Xu, W. Gao, C. Huang, S. Dou, *Chem. Soc. Rev.* **47**, 4581–4610 (2018).
 15. Y. Shao, Z. Xiao, C. Bi, Y. Yuan, J. Huang, *Nat. Commun.* **5**, 5784 (2014).
 16. Y. Hu *et al.*, *Adv. Energy Mater.* **8**, 1703057 (2018).
 17. I. Levine *et al.*, *ACS Energy Lett.* **4**, 1150–1157 (2019).
 18. C. M. Sutter-Fella *et al.*, *ACS Energy Lett.* **2**, 709–715 (2017).
 19. A. Musilenko *et al.*, *Energy Environ. Sci.* **12**, 1413–1425 (2019).
 20. E. T. Hoke *et al.*, *Chem. Sci.* **6**, 613–617 (2015).
 21. O. Hentz, Z. Zhao, S. Gradečak, *Nano Lett.* **16**, 1485–1490 (2016).
 22. C. E. Michelson, A. V. Gelatos, J. D. Cohen, *Appl. Phys. Lett.* **47**, 412–414 (1985).
 23. J. T. Heath, J. D. Cohen, W. N. Shafarman, *J. Appl. Phys.* **95**, 1000–1010 (2004).
 24. H.-S. Duan *et al.*, *Adv. Funct. Mater.* **23**, 1466–1471 (2013).
 25. Z. Chen *et al.*, *Nat. Commun.* **8**, 1890 (2017).
 26. D. Shi *et al.*, *Science* **347**, 519–522 (2015).
 27. Z. Chen *et al.*, *ACS Energy Lett.* **4**, 1258–1259 (2019).
 28. S. Yang *et al.*, *Science* **365**, 473–478 (2019).
 29. H.-S. Rao, B.-X. Chen, X.-D. Wang, D.-B. Kuang, C.-Y. Su, *Chem. Commun.* **53**, 5163–5166 (2017).
 30. W.-Q. Wu *et al.*, *Sci. Adv.* **5**, eaav8925 (2019).
 31. B. Chen, P. N. Rudd, S. Yang, Y. Yuan, J. Huang, *Chem. Soc. Rev.* **48**, 3842–3867 (2019).
 32. E. M. Tennyson, T. A. S. Doherty, S. D. Stranks, *Nat. Rev. Mater.* **4**, 573–587 (2019).
 33. Q. Wang *et al.*, *Energy Environ. Sci.* **7**, 2359–2365 (2014).
 34. Q. Jiang *et al.*, *Nat. Photonics* **13**, 460–466 (2019).
 35. T. Niu *et al.*, *Energy Environ. Sci.* **11**, 3358–3366 (2018).
- ACKNOWLEDGMENTS**
- Funding:** This work was supported by the Center for Hybrid Organic Inorganic Semiconductors for Energy (CHOISE), an Energy Frontier Research Center funded by the Office of Basic Energy Sciences, Office of Science within the U.S. Department of Energy. The study of the silicon device was supported by the Solar Energy Technologies Office (SETO) within the U.S. Department of Energy under award no. DE-EE0008749. Partial study of the single crystal growth was supported by Defense Threat Reduction Agency under Grant HDTRA1170054. **Author contributions:** J.H., Z.N., and C.B. designed the experiments. Z.N. and Y.L. synthesized the perovskite single crystals. Q.J., W.-Q.W., S.C., and B.C. fabricated the polycrystalline perovskite thin-film solar cells. B.H., Z.Y., and Z.H. fabricated the silicon solar cells. Z.N. and C.B. carried out the capacitance measurements for the devices. Z.N. conducted the solar cell simulations. S.C. and X.D. carried out electron microscope measurements for the perovskites. J.H. and Z.N. wrote the paper, and all authors reviewed the paper. **Competing interests:** None declared. **Data and materials availability:** All data needed to evaluate the conclusions in the paper are present in the paper or the supplementary materials.
- SUPPLEMENTARY MATERIALS**
- science.sciencemag.org/content/367/6484/1352/suppl/DC1
Materials and Methods
Supplementary Text
Figs. S1 to S16
Tables S1 to S3
References (36–39)
- 4 November 2019; accepted 25 February 2020
10.1126/science.aba0893

Resolving spatial and energetic distributions of trap states in metal halide perovskite solar cells

Zhenyi Ni Chunxiong Bao Ye Liu Qi Jiang Wu-Qiang Wu Shangshang Chen Xuezheng Dai Bo Chen Barry Hartweg Zhengshan Yu Zachary Holman Jinsong Huang

Science, 367 (6484), • DOI: 10.1126/science.aba0893

Mapping perovskite trap states

The high efficiency of hybrid inorganic-organic perovskite solar cells is mainly limited by defects that trap the charge carriers and lead to unproductive recombination. Ni *et al.* used drive-level capacitance profiling to map the spatial and energetic distribution of trap states in both polycrystalline and single-crystal perovskite solar cells. The interface trap densities were up to five orders of magnitude higher than the bulk trap densities. Deep traps were mainly located at the interface of perovskites and hole-transport layers, where processing created a high density of nanocrystals. These results should aid efforts aimed at avoiding trap-state formation or passivating such defects.

Science, this issue p. 1352

View the article online

<https://www.science.org/doi/10.1126/science.aba0893>

Permissions

<https://www.science.org/help/reprints-and-permissions>

Use of this article is subject to the [Terms of service](#)